


Quantum light-field microscopy for volumetric imaging with extreme depth of field

Yingwen Zhang^{1,2,*}, Duncan England^{2,†}, Antony Orth², Ebrahim Karimi^{1,2} and Benjamin Sussman^{1,2}

¹*Nexus for Quantum Technologies, University of Ottawa, Ottawa, Ontario K1N 6N5*

²*National Research Council of Canada, 100 Sussex Drive, Ottawa, Ontario K1A0R6, Canada*

 (Received 11 October 2023; revised 24 October 2023; accepted 25 January 2024; published 14 February 2024)

Light-field microscopy (LFM) is a three-dimensional microscopy technique whereby volumetric information of a sample is gained by simultaneously capturing both the position and momentum information of light illuminating the sample. Conventional LFM designs generally require a trade-off between position and momentum resolution, requiring one to sacrifice resolving power for increased depth of field (DOF). In this work, we demonstrate a LFM design that does not require this trade-off by utilizing the inherent correlations between spatial-temporal entangled photon pairs. Here, one photon from the pair is used to illuminate a sample from which the position information of the photon is captured directly by a camera. By virtue of the momentum anticorrelation between the two photons, the momentum information of the illumination photon can be inferred by measuring the momentum of its entangled partner. By using a wave-optics approach for the light-field reconstruction, we demonstrate that a resolving power of up to 5 μm can be maintained with a DOF of approximately 500 μm , approximately 10 times that of a conventional LFM or > 100 times that of a bright-field microscope. In the extreme, at a resolving power of 100 μm , it is possible to achieve near infinite DOF.

DOI: [10.1103/PhysRevApplied.21.024029](https://doi.org/10.1103/PhysRevApplied.21.024029)

I. INTRODUCTION

Utilizing the properties of quantum entangled photons to enhance the performance of sensing and imaging techniques has been an active area of research in recent decades. To date, most demonstrated techniques are focused on noise reduction in the low illumination regime by utilizing the strong correlations in one of the many degrees of freedom between entangled photon pairs, such as in time or position and momentum. Examples of this are subshot noise imaging [1,2] and quantum ghost imaging [3–5]. Dispersion immune optical coherence tomography has also been demonstrated using the two-photon Hong-Ou-Mandel interference effect [6,7]. With advances in detector technology, especially with the maturity of single-photon-sensitive event cameras [8,9], it is now possible to simultaneously utilize the correlations between multiple degrees of freedom. It has been demonstrated for further enhanced noise reduction in imaging and sensing by utilizing spectral-temporal correlations [10] or spatial-temporal correlations [9,11] in entangled photons. Other quantum imaging techniques utilizing the quantum correlations in multiple degrees of freedom have also been demonstrated,

such as snapshot hyperspectral imaging [12], phase imaging through phase-contrast microscopy [13] and Fourier ptychography [14], Hong-Ou-Mandel-microscopy [15], as well as light-field or plenoptic imaging [16]. In this work, we extend the quantum correlation light-field imaging design [16] to microscopy and demonstrate volumetric reconstruction of a microscopic scene at the few micron resolution with extreme depth of field (DOF).

Light-field or plenoptic imaging [17–19] is a class of imaging techniques, which allows for the reconstruction of the light field through capturing both the position and momentum (angular) information of light rays simultaneously. With the reconstructed light field, volumetric information of an illuminated scene can be obtained in a single measurement, with no scanning required. This technique has since been adapted to microscopy [20,21], and has been demonstrated in volumetric non-scanning imaging of neural activities [22], microendoscopy [23] and also shown to have potential applications in optogenetics [24]. Conventional light-field microscope (LFM) designs typically make use of a microlens array (MLA). By placing the MLA one focal length away from an image sensor, each microlens illuminates a subset of the pixels in the CCD. By knowing which lens the light ray enters, and onto which pixel it subsequently focuses, one can obtain both position and momentum information of the light ray simultaneously, at the expense of sacrificing spatial

*yzhang6@uottawa.ca

†Duncan.England@nrc-cnrc.gc.ca

resolution to gain momentum resolution. Typical LFM designs have each microlens covering around 10×10 pixels, thus resulting in a 10 times reduction to the position resolution and subsequently, resolving power. Increasing the size of each microlens to cover more pixels will increase the amount of momentum information captured and subsequently increase the DOF, however at the cost of further reduced position resolution. Techniques have been developed to improve either the DOF or resolving power such as through scanning the MLA [25] or the sample stage [26]. Others include applying three-dimensional (3D) deconvolution [27], wave-front shaping [28], using a camera array [29], processing the light-field information through the Fourier domain [30], or using the aid of spherical aberrations in scanning LFM [31].

In recent years, an alternative light-field imaging technique using spatially correlated thermal or quantum light has been proposed [32–34]. Here one beam or photon illuminates a scene to capture the position information, and the momentum information is inferred from the correlated partner beam or photon that is measured on a separate camera. Using this method, no trade-off between the position and momentum resolution is needed since each beam can be captured on separate cameras thus allowing for a much larger DOF while not sacrificing resolving power. This technique has since been demonstrated using a ray optics approach with weakly correlated thermal light [35–37] and quantum-correlated light [16], with a DOF at around 10 mm for a resolving power in the order of $100 \mu\text{m}$.

In this work, we present a proof-of-concept demonstration of light-field microscopy using quantum correlated photons. We refer to this technique as quantum correlation light-field microscopy (QCLFM) throughout the rest of the paper. Unlike the previous work [16] that employed only ray optics, we utilize a wave optics approach in order to account for the diffraction effects that result from the much smaller target features. Our results demonstrate a resolving power of up to $5 \mu\text{m}$ (200 lp/mm —line pairs per millimeter), with a depth of field (DOF) of approximately $500 \mu\text{m}$. At a resolving power of up to $10 \mu\text{m}$ (100 lp/mm), the DOF can be extended to over 1.5 mm. This DOF is > 100 times that of a conventional microscope using the same objective lens. Compared to LFM designs, this is almost 20 times larger compared to the first LFM demonstration [20] and is between 3 to 10 times larger compared to some of the more recent LFM demonstrations [27,28,31] where various advanced imaging processing techniques were used. In the extreme case, at a resolving power of $100 \mu\text{m}$, we observed a near infinite DOF, a feat that is practically unfeasible with current LFM designs based on MLA.

II. EXPERIMENTAL SETUP

The schematic of our QCLFM setup is shown in Fig. 1(a). A fiber-coupled 405-nm cw laser (TOPTICA iBeam smart), at approximately 30 mW, is used to pump a $1 \times 2 \times 1 \text{ mm}$ ($H \times W \times L$) type-II periodically poled

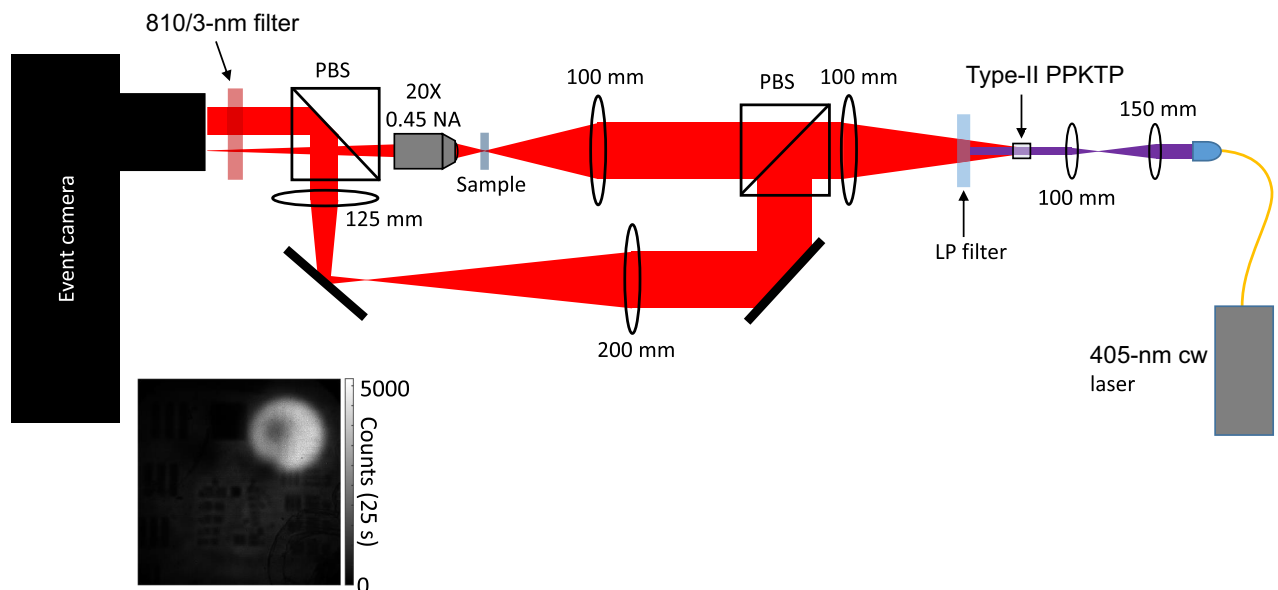


FIG. 1. Experimental setup of QCLFM. PBS, polarizing beam splitter; LP filter, long-pass filter; PPKTP, periodically poled potassium titanyl phosphate crystal. The inset shows a typical image captured on the camera, before time correlation analysis, accumulated over 25 s. The signal beam covers the whole sensor area, while the idler is the bright region on the top-right corner. The idler beam on the corner is seen much brighter compared to the signal beam covering the whole sensor, this is due to a similar amount of photons being concentrated onto a smaller area. The darker patch seen in the idler beam is due to a damaged region on the camera system resulting in lower detection efficiency.

potassium titanyl phosphate (PPKTP) crystal (Raicol Crystals) to produce entangled photon pairs through SPDC, at a rate of approximately 15×10^6 photon pairs per second or, after accounting for the 7% camera detection efficiency, about 15 photons per second per pixel detected on the camera. Here, we have limited the photon-pair production rate by not using a higher pump power so as to not saturate the camera. The photon pairs are orthogonal in polarization, correlated in position, momentum, and time. The SPDC photons are then separated by a polarizing beam splitter (PBS) into two paths. In the path of the signal photon, the plane of the crystal is first imaged onto the sample placement region and then onto a time-tagging event camera (TPX3CAM [8,38]) to record the signal photon's position information and arrival time. In the path of the idler photon, the Fourier plane of the crystal is projected onto a corner of the camera to record the idler photons' momentum information and the subsequent arrival time. Thus, the position information of the signal photon is captured directly and its momentum information can be inferred from the idler partner. The photon pairs are identified through a time-correlation measurement, with a coincidence gating time of 10 ns, on all photons detected between the idler beam region and the rest of the camera. Though the idler beam is overlapped with part of the signal beam on the camera, since a time-correlation measurement is performed, the noise in accidental coincidences from this overlap is very low. This is because the probability of having two signal photons generated within the 10-ns coincidence gating time is very low. More details on the operation of the camera and measuring of the momentum correlation can be found in the [Appendix](#).

III. DIGITAL REFOCUSING PROCEDURE

Using the position and momentum information of each photon, the operation for digital refocusing of a sample placed out of focus by a distance z can be achieved using two steps. First, the trajectory of the photons are determined through ray tracing using a ray transfer matrix

$$\begin{bmatrix} \vec{r}_2 \\ \vec{\theta}_2 \end{bmatrix} = \begin{bmatrix} A & B \\ C & D \end{bmatrix} \begin{bmatrix} \vec{r}_1 \\ \vec{\theta}_1 \end{bmatrix}, \quad (1)$$

where \vec{r}_1 and \vec{r}_2 are the positions of each photon pair detected at the two camera image planes, $\vec{\theta}_1$ and $\vec{\theta}_2$ are the angles at which the photons hit each plane and the ray transfer ($ABCD$) matrix is determined by the optical components placed between the two image planes. Since \vec{r}_1 and \vec{r}_2 are measured directly by the two cameras and the $ABCD$ matrix is also known, $\vec{\theta}_1$ and $\vec{\theta}_2$ can be determined from Eq. (1). Knowing \vec{r} and $\vec{\theta}$, an appropriate $ABCD$ matrix is then used to digitally propagate each photon to the location of the sample.

For large features, where diffraction effects are negligible, this first step, using ray optics, is enough to bring the sample back into focus [16], however, for smaller features, interference and diffraction effects from wave optics must also be taken into account. In this case, the image obtained after ray tracing is the diffraction-pattern amplitude of the sample at a distance z when illuminated by a plane wave propagating in the z direction (see the [Appendix](#) for details). A Gerchberg-Saxton-type algorithm [39,40] can then be used to recover the amplitude of the sample provided the phase profile of the sample is constant or known. The traditional Gerchberg-Saxton algorithm [39,40] uses the amplitude information obtained at the image plane and Fourier plane to retrieve the phase information of the two through the Fourier transform relation between the two planes. Here, we use the amplitude of an arbitrary plane and the phase of another to retrieve the corresponding missing phase and amplitude of the two planes. The relationship between the two planes is no longer a direct Fourier transform but that of wave diffraction where techniques for approximating wave diffraction, such as the angular spectrum method or Fresnel diffraction method, must be used. The algorithm is illustrated in Fig. 2 and works as follows:

- (1) Guess an initial phase profile for the diffraction-pattern amplitude obtained after ray tracing (a flat initial phase was used here).
- (2) Apply the angular spectrum method to the diffraction pattern to reverse diffraction and obtain an amplitude and phase profile of the sample [Fig. 2(b1) to (b2)].
- (3) Replace the phase profile of the sample obtained from (2) with the known phase profile (which is zero for the targets used in this experiment) [Fig. 2(b2) to (b3)] and then apply the angular spectrum method to obtain the amplitude and phase of its diffraction pattern [Fig. 2(b3) to (b4)].
- (4) Update the diffraction pattern obtained from ray tracing with the updated phase profile [Fig. 2(b4) to (b1)].
- (5) Repeat the process from step (2).

The angular spectrum method is applied as follows, for a beam with an initial amplitude and phase profile of $U_i(x,y)e^{i\phi_i(x,y)}$, the profile after propagating a distance z is

$$U_f(x,y)e^{i\phi_f(x,y)} = \mathcal{F}^{-1} [\mathcal{F} (U_i(x,y)e^{i\phi_i(x,y)}) e^{ik_z z}], \quad (2)$$

where \mathcal{F} (\mathcal{F}^{-1}) denotes the (inverse) Fourier-transform operation and $k_z = \sqrt{k^2 - k_x^2 - k_y^2}$ with $k = 2\pi/\lambda$ being the photon wave number.

Because step (3) in the above algorithm assumes a known phase profile (assumed to be flat in this case), the refocusing procedure is extremely sensitive to phase gradients introduced by the sample. Accordingly, this technique

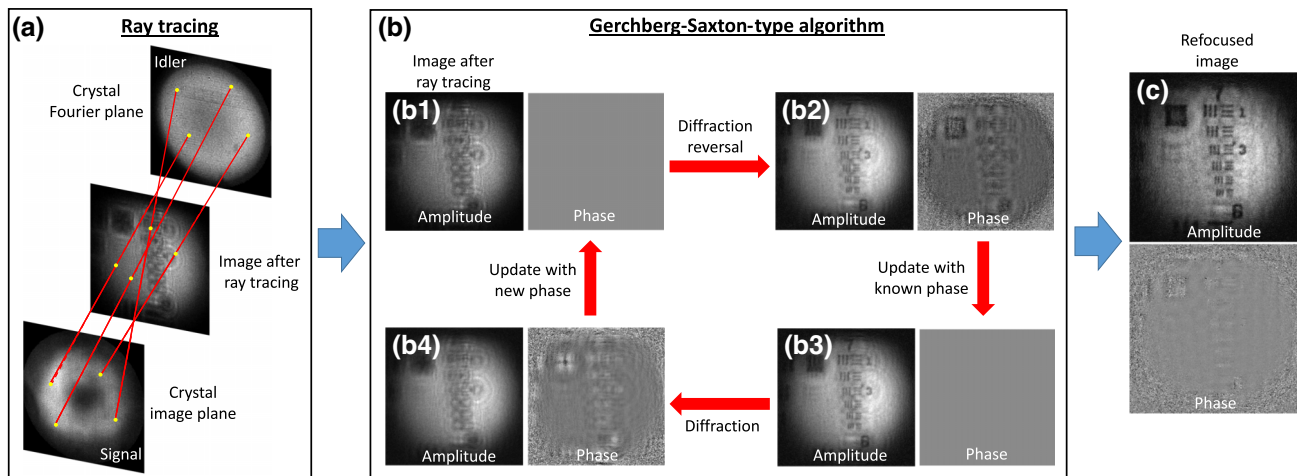


FIG. 2. Illustration of the digital refocusing process. (a) Using the photon-pair locations detected on the nonlinear crystal’s image plane and Fourier plane, a ray-tracing approach is first used to obtain the diffraction pattern amplitude of the sample as if illuminated by a plane-wave propagating in the z direction. (b) For a sample of uniform or known phase profile, a Gerchberg-Saxton type algorithm is used to recover the amplitude profile of the sample. (c) The recovered amplitude and phase of the sample after 10 loops in the algorithm. This illustration is that of a 1951 USAF resolution target (group 7) placed at $z = -300 \mu\text{m}$ away from the focus of the microscope objective.

is most suited to the samples with a flat phase profile such as the microscope resolution target shown in Fig. 3. A more realistic type of target to which this technique can be applied is shown in Fig. 4 where opaque objects are sparsely distributed across the sample volume. Imaging of more complex scenes with nontrivial phase profiles will require improved imaging and processing techniques. This will be the focus of future works.

Here, the processing of raw camera data involves two steps. The first step is to identify and calculate the centroids of pixel clusters, followed by the identification of photon pairs through time-correlation analysis as detailed in Refs. [8,41]. This process needs only to be executed once on the raw data. Utilizing the latest Intel i5 CPU with 14 processing cores, it takes approximately 5 s to process 1 s of raw data of which 90% of the process time is used for the clustering and centroiding analysis. To achieve real-time postprocessing, the process can be further parallelized by leveraging GPU computing. Another is to use a different type of time tagging single-photon camera system, which does not require this clustering and centroiding analysis, such as some SPAD array cameras [42]. Currently, these event-based SPAD-array cameras are still in early development and does not have a high enough pixel resolution and effective quantum efficiency (after accounting for the fill factor) to compete with the TPX3CAM, however, with the rapid development of single-photon detection technologies, we believe they will become a viable alternative in the near future.

The second step involves the refocusing process, performed on the now identified photon-pair events. Using the same i5 CPU, performing the above digital refocusing

procedure can be accomplished in 0.75 s. The majority of the processing time is consumed by ray tracing the millions of photon-pair events, while the Gerchberg-Saxton algorithm, performed up to 10 loops, accounts for only about 20% of the total processing time. With additional optimization and a faster CPU, it is indeed possible to achieve even faster processing times for this step.

IV. RESULTS

In Fig. 3 we show digitally refocused images of a 1951 USAF resolution target placed at different distances from the objective focus. For identifying the transverse resolution, we take the cross section of the triplet lines of the resolution target and determine its visibility defined as $(I_{\text{max}} - I_{\text{min}})/(I_{\text{max}} + I_{\text{min}})$, where I_{max} is the average maximum intensity of the bright region between the triplet bars and I_{min} is the average minimum intensity of the dark region between the bars. If the visibility in one orientation of the triplet lines, whether vertical or horizontal, is greater than zero by more than the error bar then we consider it as resolved (see the Appendix for more details). We see that a line spacing of $5 \mu\text{m}$ (group 7 element 5) can still be brought back into focus when the target is placed $\pm 500 \mu\text{m}$ away from the focus of the objective lens (positive being towards the objective lens and negative being away from) and for a line spacing of $10 \mu\text{m}$ (group 6 element 5) this distance can be extended to more than $1500 \mu\text{m}$. In the extreme case, we are able to refocus a target placed at -1.75 cm away from the focus with a line spacing of approximately $100 \mu\text{m}$, as seen in Fig. 3(c), which is very close to the Fourier plane, i.e., near infinity. This is verified

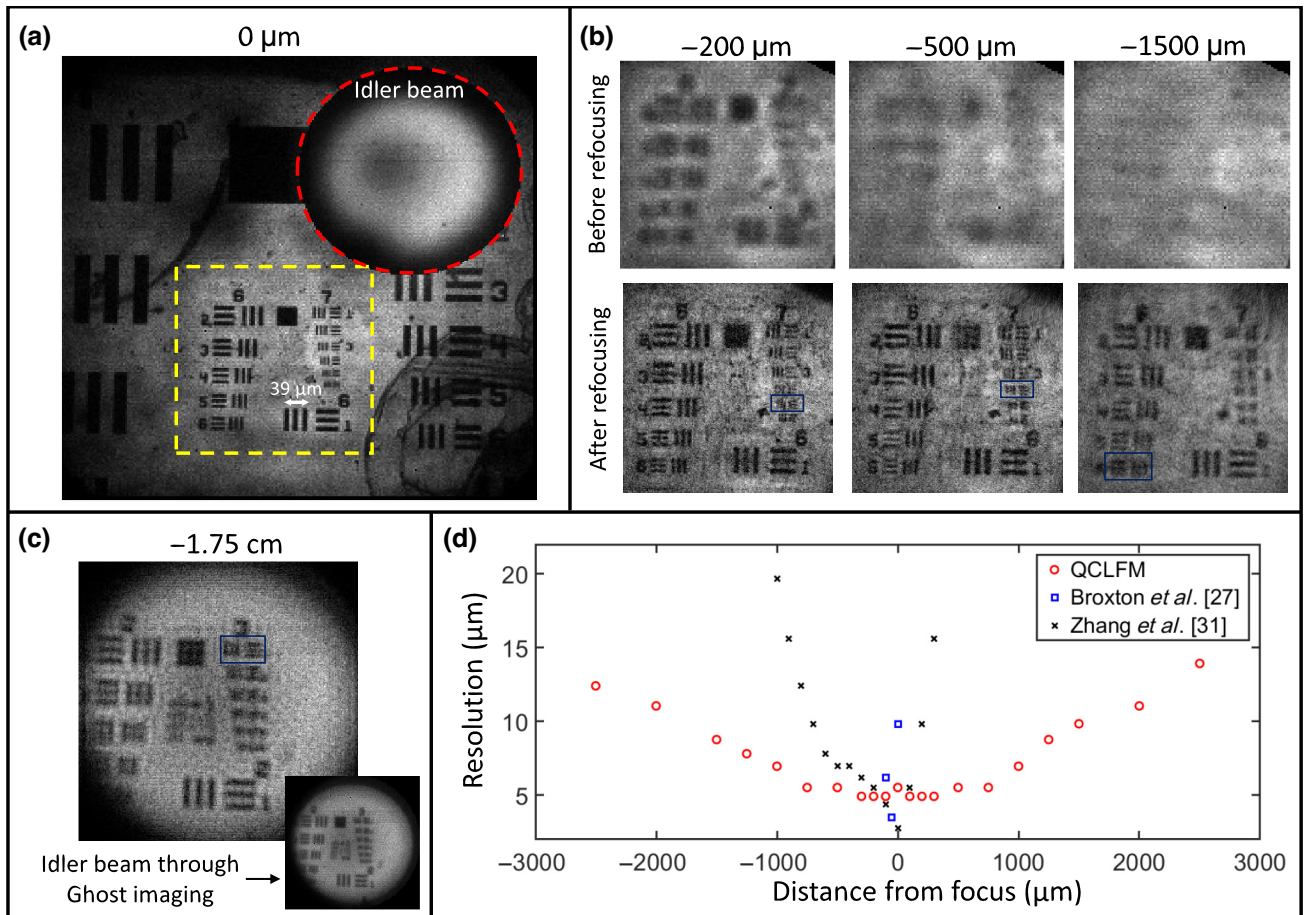


FIG. 3. Refocusing of 1951 USAF resolution target (a) Image of a 1951 USAF resolution target, obtained after time correlation measurement, placed in the focus of a 20×0.45 NA objective lens. Here, for every photon detected in the idler beam, there is a signal photon detected in coincidence in the rest of the image. The region circled in red is the far field imaged by the idler photons. To not overshadow the rest of the image, the idler beam is only displayed at 30% intensity. (b) Images before and after digitally refocusing groups 6 and 7 of 1951 USAF target [region in yellow square of (a)]. Refocusing is performed for the target placed at different distances from the objective focal plane, with smallest resolvable features after refocusing boxed in blue. The data acquisition time for the images is 200 s. (c) Digital refocusing of USAF target groups 2 and 3 placed 1.75 cm away from the focus with a slightly different lens configuration. This is very close to the Fourier plane as the target can be clearly seen through ghost imaging in the idler beam (inset). See the main text for an explanation of ghost imaging. (d) Plot showing the minimum resolvable feature size with respect to target distance in the context of QCLFM and conventional LFM demonstrations [27,31]. Positive distance is towards the objective lens and negative is away from the lens. See the Appendix for the full dataset of (b),(c),(d).

through ghost imaging [3–5], a correlation imaging technique using pairs of photons, in which the idler photon does not interact with the target being imaged, with only the signal photon interacting with the target. By time correlating the detection events of the two photons, an image of the object will appear through the idler photons even though they did not directly interact with the target. Knowing the idler beam is imaged in the crystal’s Fourier plane, being able to see the target clearly after time-correlation measurement is an indicator that the target is also placed at or near the Fourier plane.

In Fig. 3(d), we also compared QCLFM with MLA-based conventional LFM demonstrations that have a similar resolving power. We achieved around an order of

magnitude improvement in DOF as compared to the first conventional LFM, which utilized wave optics [27] (group 7 element 3 with 1000- μm DOF compared to 100- μm DOF). Compared to one of the latest LFM demonstrations [31], which incorporated the use of additional tools such as image plane scanning and spherical aberration assistance, a 3 times improvement in DOF is still observed (group 7 element 3 with 1000- μm DOF compared to 300- μm DOF and group 6 element 3 with 2000- μm DOF compared to 800- μm DOF). See the Appendix for a direct comparison between the images from the various techniques. Comparing to the first LFM demonstration [20], in which only a ray-optics approach was used, the DOF improvement offered by QCLFM is almost 20 times

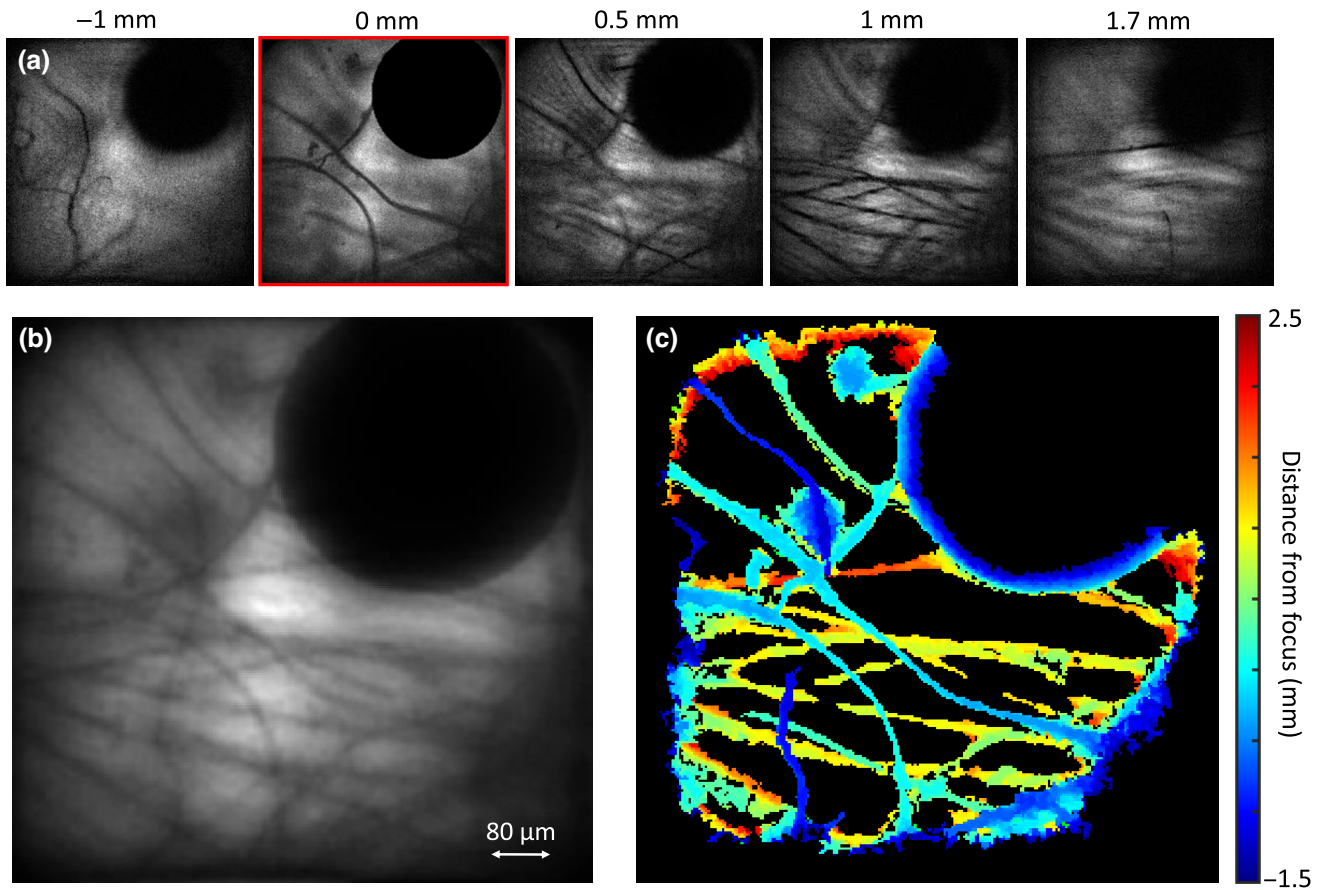


FIG. 4. Refocusing of lens tissue fiber. (a) Digitally refocusing onto fiber strands of lens-cleaning tissue at various distances from the focus of the objective lens. The image at the lens focus is highlighted in red. The fiber strands are from the edges of an approximately 3-mm-thick stack of lens-cleaning tissue. The measurement is taken in with a data acquisition time of 200 s. The empty circular region on the top right is the part of the camera used for capturing the idler photons. (b) Image showing all fiber strands brought into focus through summing all the refocused images at each depth slice. (c) Depth map of the fiber strands. A video showing the refocused images at different depths can be found in the [Appendix](#).

(10- μm resolution with 2000- μm DOF compared to 120- μm DOF). In addition, we see that QCLFM is also insensitive to the direction at which the target is placed from the objective focus as compared to some conventional LFM techniques [27,31].

The reduction in resolving power with increased distance at which a sample is placed from the objective focus, as seen in Fig. 3(d), is a direct consequence of the decrease in the effective numerical aperture of the imaging system. When the sample is positioned closer to or farther away from the designed focal plane of the objective lens, the diffracted light rays from the sample containing higher spatial frequency features will fall outside the optimal acceptance angle of the objective lens. As a result, the resolution is diminished as the object moves away from the focus, an effect which is common to all LFM techniques.

It is informative to also determine the axial resolution of QCLFM. To do this, we keep the physical position of the target fixed at a point, which is not in the focal plane,

and digitally change the focusing by adjusting the depth parameter in our refocusing algorithm to see where the digitally refocused target becomes unresolvable again. We then compared this digital defocusing distance to a conventional microscope, constructed using the same lenses, where the target is now physically moved from the focus until it becomes unresolvable. Comparing the physical and digital focal scans we see that the axial resolution of QCLFM is comparable to the DOF of a conventional microscope constructed with the same lenses. For further details, and a comprehensive analysis, refer to the [Appendix](#).

Next, we test our technique on a more complex 3D scene. Imaging of multiple overlapping fiber strands, between 5–10 μm in diameter, on the edges of an approximately 3-mm-thick stack of lens-cleaning tissue can be seen in Fig. 4. A single measurement was taken on the stack of lens tissue with digital refocusing performed in postprocessing. We can see fiber strands more than 1 mm

away from the objective lens focus, and completely not visible at the objective focus, being brought back into focus. The postprocessing results in a stack of in-focus images obtained at various depths in the sample, some examples of which are shown in Fig. 4(a). The sum of all of these depth images results in an “all in focus” image [Fig. 4(b)] in which every strand, regardless of its position, is brought into focus. Finally, by color-coding each image based on its depth, we generate a depth map of the 3D scene shown in Fig. 4(c). A video showing the refocused images at different depths can be found in the [Appendix](#).

Some artifacts and halos can be seen in the refocused images, this is likely a result of wave-front distortions from the multiple lenses used in the setup, which were not taken into account during the refocusing procedure. Another likely source is in the approximations made in the refocusing procedure, such as using small angle approximations and assuming a uniform illumination beam intensity (see the [Appendix](#) for details).

The DOF of LFM at a particular resolving power is in large determined by the number of measurable momenta spots. To fully utilize the approximately 100×100 pixels assigned for momentum measurement, a one-to-one momentum correlation between the two photons is desired. In such a scenario, measuring the momentum of the idler photon would precisely determine the momentum of the signal photon. However, in practice, the momentum correlation distribution is affected by various factors. These include the coherence length and beam waist of the pump laser, the collimation of the pump laser at the crystal, and the wavelength of the SPDC photons. For the specific SPDC source utilized in this experiment, the momentum correlation has been measured to be approximately $12 \times 10^{-3} \text{ um}^{-1}$ or 1.8 pixels wide (refer to the [Appendix](#) for detailed information). Consequently, this introduces an uncertainty of 1.8 pixels in the momentum of the signal photon, given a measured momentum of its correlated idler photon. As a result, the momentum resolution is effectively reduced from the initially assigned approximately 100×100 pixels to around 50×50 distinct momenta spots. To enhance the momentum correlation of SPDC, and further improve the performance of QCLFM, the simplest method is to use a pump laser with longer coherence length.

V. DISCUSSION

We have made a proof-of-concept demonstration of a LFM design based on utilizing the inherent position and momentum correlation of entangled photon pairs generated through the process of SPDC. Since each degree of freedom can potentially be measured on separate cameras, one does not need to sacrifice position resolution for momentum resolution or vice versa as in conventional MLA-based LFM designs. This has allowed us to achieve a DOF that is approximately 3 times larger than that of

the latest LFM designs, all at an illumination power of about 3 pW (15×10^6 photons per second at 810 nm). With the high momentum resolution (effectively approximately 50×50 pixels at 13.8 um^{-1} per pixel), it is even possible to digitally refocus objects placed at near infinity, though with a moderate resolving power. In addition, as compared to some conventional LFM techniques, QCLFM is also insensitive to whether the target is placed before or after the objective focus. For a MLA-based LFM design to achieve a comparable 4D position-momentum resolution of this initial QCLFM demonstration will require a camera with > 150 megapixels, a number well beyond what is commercially available.

As noted in the original proposal [32], and demonstrated in subsequent experimental works [35–37], light-field imaging based on the intensity correlation of speckle patterns in thermal light can only operate in the ray-optics regime. On the other hand, if working in the single-photon regime, one could rely upon the weak-bunching nature of thermal light as a replacement for SPDC to perform LFM using the approach as presented in this work. However, due to the SNR being dependant on the second-order correlation strength $g(2)$, thermal light, which have a $g(2)$ bounded at 2, will perform at a worse SNR than SPDC, which typically can achieve much higher values of $g(2)$ [43]. The $g(2)$ of our SPDC source measured through the camera is 8.

The DOF can be further increased if a higher degree of momentum correlation is achieved and using a separate camera for the momentum measurement on the idler photon. Momentum correlation can be improved by increasing the pump beam waist or using a pump with a longer coherence length. Position resolution can be further improved by a factor of 3 on the event camera (TPX3CAM) using centroiding techniques [44]. QCLFM utilizes only the strong correlations inherent in spontaneous parametric down-conversion, and does not leverage photon entanglement. Thus it is possible to imagine combining QCLFM with other quantum sensing techniques, which directly utilize entanglement, such as quantum lithography [45,46], to achieve resolution beyond the diffraction limit. Additionally, the current QCLFM design is still in its most basic form, we believe significant performance gains can be made by incorporating more sophisticated tools already developed for the conventional LFM design, such as wave-front shaping [28] and spherical aberration assistance [31].

Currently, a major limitation to the technique’s performance (as with all single-photon quantum imaging techniques, in general) is in its slow data-acquisition speed, which requires on the order of a few hundred seconds. Though this is relatively short compared to many other quantum imaging demonstrations, which often requires hours of data taking, it is still much slower as compared to the 10–100 Hz frame rate of conventional LFM. This is mainly limited by the detection efficiency and timing

resolution of the detection camera. The single-photon detection efficiency of the camera used is approximately 7% with an effective timing resolution of approximately 8 ns [41]. Since the pair-detection efficiency is quadratic with respect to the single-photon detection efficiency, with a camera efficiency of 50%, we could expect a $(50/7)^2 \approx 50$ times improvement in the data-acquisition speed. Moreover, the signal-to-noise ratio of temporal correlation measurement scales as the square root of the timing resolution, so if a timing resolution of 0.1 ns can be achieved, a further 10 times reduction to the data-acquisition time is possible. Single-photon avalanche photodiode array cameras meeting these specifications are already in development and may become commercially available soon [47]. We expect this will make real-time imaging and microscopy with QCLFM (and many other quantum imaging techniques) a possibility in the near future.

ACKNOWLEDGMENTS

The authors are grateful to Denis Guay, and Doug Moffatt for technical support. The authors acknowledge the support of Canada Research Chair, NRC-uOttawa Joint Centre for Extreme Quantum Photonics (JCEP), Quantum Sensors Challenge Program at the National Research Council of Canada and Defence Research and Development Canada.

APPENDIX A: REFOCUSING OPERATION

For a plane wave traveling in an arbitrary direction $U(x, y, z) = Ae^{i(ux+vy+wz)}$ (with $2\pi/\lambda = k = \sqrt{u^2 + v^2 + w^2}$) illuminating a target with complex spatial profile $f(x, y) = \mathcal{F}^{-1}[F(k_x/2\pi, k_y/2\pi)]$ (\mathcal{F} denoting the Fourier transform operation) placed at $z = 0$, the transmitted wave can then be written as a superposition of plane waves (also known as the angular spectrum method) given by

$$\begin{aligned} U_T(x, y, z) &= \frac{1}{4\pi^2} \int \int_{-\infty}^{\infty} F(k_x/2\pi, k_y/2\pi) e^{i(k_x x + k_y y)} \\ &\quad \times U(x, y, 0) e^{i\tilde{k}_z z} dk_x dk_y \\ &= \mathcal{F}^{-1} \left[F(k_x/2\pi, k_y/2\pi) e^{i(\tilde{k}_z z)} \right] U(x, y, 0), \end{aligned} \quad (\text{A1})$$

with $\tilde{k}_z = \sqrt{k^2 - (k_x + u)^2 - (k_y + v)^2}$.

In the case of small angle approximation where the x and y components of the k vector is much smaller than the z component, we can approximate \tilde{k}_z using a Taylor-series expansion

$$\begin{aligned} \tilde{k}_z &= \sqrt{k^2 - k_x^2 - k_y^2 - 2k_x u - 2k_y v - u^2 - v^2} \\ &\approx k_z - \frac{k_x u + k_y v}{k_z} + O(u^2, v^2), \end{aligned} \quad (\text{A2})$$

where $k_z = \sqrt{k^2 - k_x^2 - k_y^2}$.

Now substituting back into Eq. (A1) we have

$$\begin{aligned} U_T(x, y, z) &\approx \mathcal{F}^{-1} \left[F(k_x/2\pi, k_y/2\pi) e^{i\left(k_z - \frac{k_x u + k_y v}{k_z}\right)z} \right] U(x, y, 0) \\ &= \mathcal{F}^{-1} \left\{ \mathcal{F} [f(x - \Delta x, y - \Delta y)] e^{ik_z z} \right\} U(x, y, 0) \\ &= \tilde{f}(x - \Delta x, y - \Delta y, z) U(x, y, 0), \end{aligned} \quad (\text{A3})$$

where we have used the Fourier-transform property $\mathcal{F} [f(x - \Delta x)] = F(k_x/2\pi) e^{-ik_x \Delta x}$ with $\Delta x = uz/k_z$ and $\Delta y = vz/k_z$ and $\tilde{f}(x, y, z) \equiv \mathcal{F}^{-1} \left\{ \mathcal{F} [f(x, y)] e^{ik_z z} \right\}$ is the diffracted field of a target $f(x, y)$ illuminated by a plane wave traveling in the z direction.

For this experiment, there are an infinite number of plane waves illuminating the target of which we are able to measure a total of $N \times M$, the total number of pixels used to capture the idler photons in the far-field plane. Thus we will denote the transmitted wave associated with a particular far-field pixel, with pixel index n and m in the x and y direction, respectively, as $U_{Tnm}(x, y, z) = \tilde{f}(x - \Delta x_n, y - \Delta y_m, z) U_{nm}(x, y, 0)$ with $U_{nm}(x, y, 0) = A_{nm} e^{i(u_n x + v_m y)}$. The captured image in the near-field plane $I_0(x, y, z_0)$ is thus given by the sum of all the transmitted waves squared, i.e.,

$$I_0(x, y, z_0) = \left| \sum_{n,m} \tilde{f}(x - \Delta x_n, y - \Delta y_m, z_0) U_{nm}(x, y, 0) \right|^2. \quad (\text{A4})$$

Since we can track each photon in forming $I_0(x, y, z_0)$ from the far-field to the near-field plane, we can break up $I_0(x, y, z_0)$ into a total of $N \times M$ individual images $\tilde{I}_{nm}(x, y, z_0)$ for each (u_n, v_m) pixel in the far field thus

$$\begin{aligned} I_0(x, y, z_0) &= \sum_{n,m} \tilde{I}_{nm}(x, y, z_0) \\ &= \left| \sum_{n,m} \tilde{f}(x - \Delta x_n, y - \Delta y_m, z_0) U_{nm}(x, y, 0) \right|^2. \end{aligned} \quad (\text{A5})$$

Making a coordinate shift gives

$$\begin{aligned} &\sum_{n,m} \tilde{I}_{nm}(x + \Delta x_n, y + \Delta y_m, z_0) \\ &= \left| \sum_{n,m} \tilde{f}(x, y, z_0) U_{nm}(x + \Delta x_n, y + \Delta y_m, 0) \right|^2 \\ &= \left| \tilde{f}(x, y, z_0) \right|^2 \left| \sum_{n,m} U_{nm}(x + \Delta x_n, y + \Delta y_m, 0) \right|^2. \end{aligned} \quad (\text{A6})$$

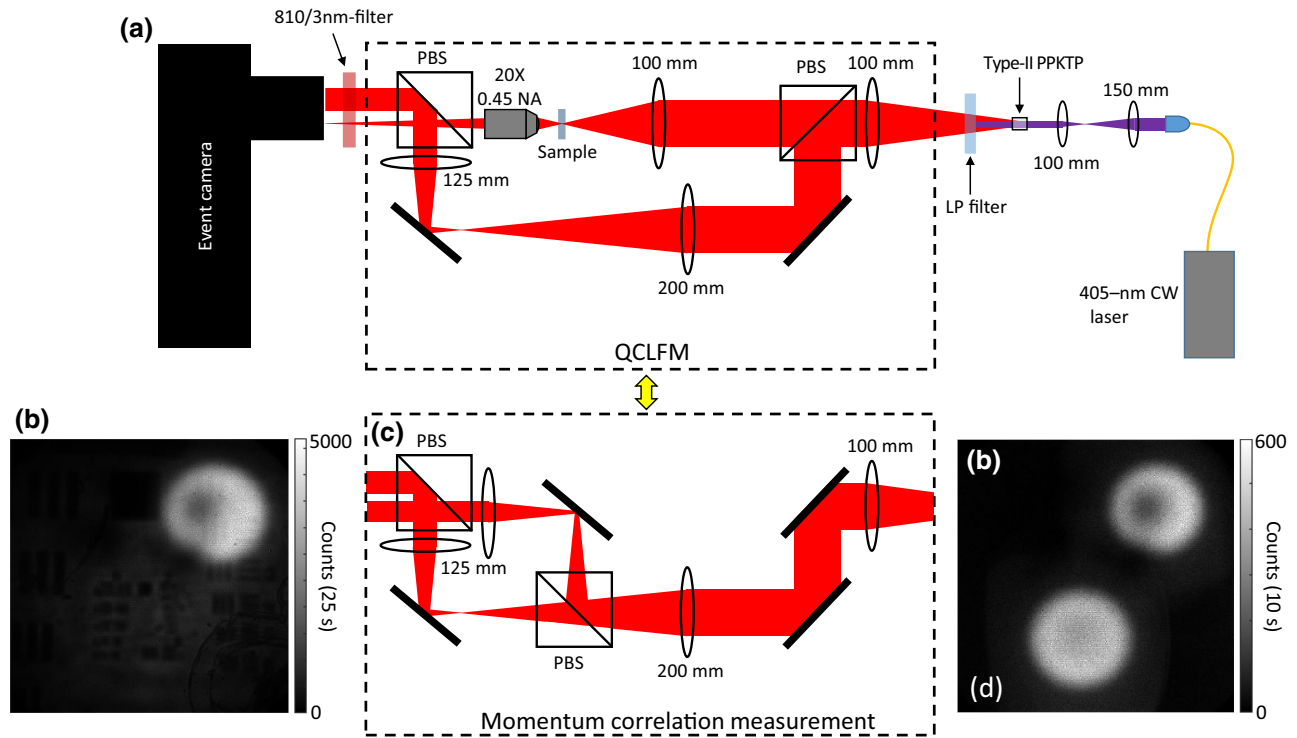


FIG. 5. Experimental setup of QCLFM. (a) Experimental setup of the QCLFM. PBS, polarizing beam splitter; LP filter, long-pass filter. (b) A typical image captured on the camera, before time-correlation analysis, accumulated over 25 s, of a 1951 USAF resolution target placed 200 μm away from the objective focus. The signal beam covers the whole sensor area, while the idler is the bright region on the top-right corner. (c) The modified experimental setup for performing momentum correlation measurement. (d) Image captured on the camera, before time-correlation analysis, accumulated over 10 s, for performing momentum correlation measurement. The darker patch seen in the idler beam in both (b),(d) is due to a damaged region on the camera system resulting in lower detection efficiency.

On the left side of Eq. (A6), the operation of shifting each image \tilde{I}_{mm} by a distance of $\Delta x_n = u_n z_0 / k_z$ and $\Delta y_m = v_m z_0 / k_z$ in the x - y plane is equivalent to the

ray-tracing operation of shifting the position of each photon by the same factor based on the direction the photon is traveling given by $\theta_x \approx u_n / k_z$ and $\theta_y \approx v_m / k_z$ after

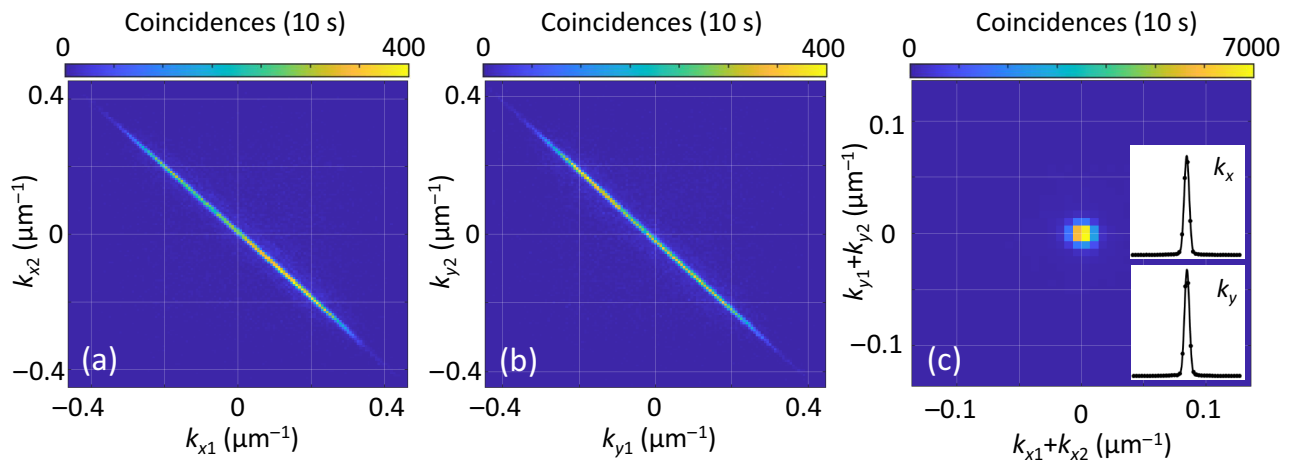


FIG. 6. Momentum correlation measurement. (a) Joint probability distribution of photon momentum in the x direction k_x . (b) Joint probability distribution of photon momentum in the y direction k_y . (c) Sum coordinate projection of the joint probability distribution with the fitted Gaussian to the cross section of the k_x and k_y direction shown in the inset. Fitted Gaussian gives $\sigma_{k_{x1}+k_{x2}} = 6.1 \times 10^{-3} \mu\text{m}^{-1}$ (0.90 pixels) and $\sigma_{k_{y1}+k_{y2}} = 6.4 \times 10^{-3} \mu\text{m}^{-1}$ (0.93 pixels).

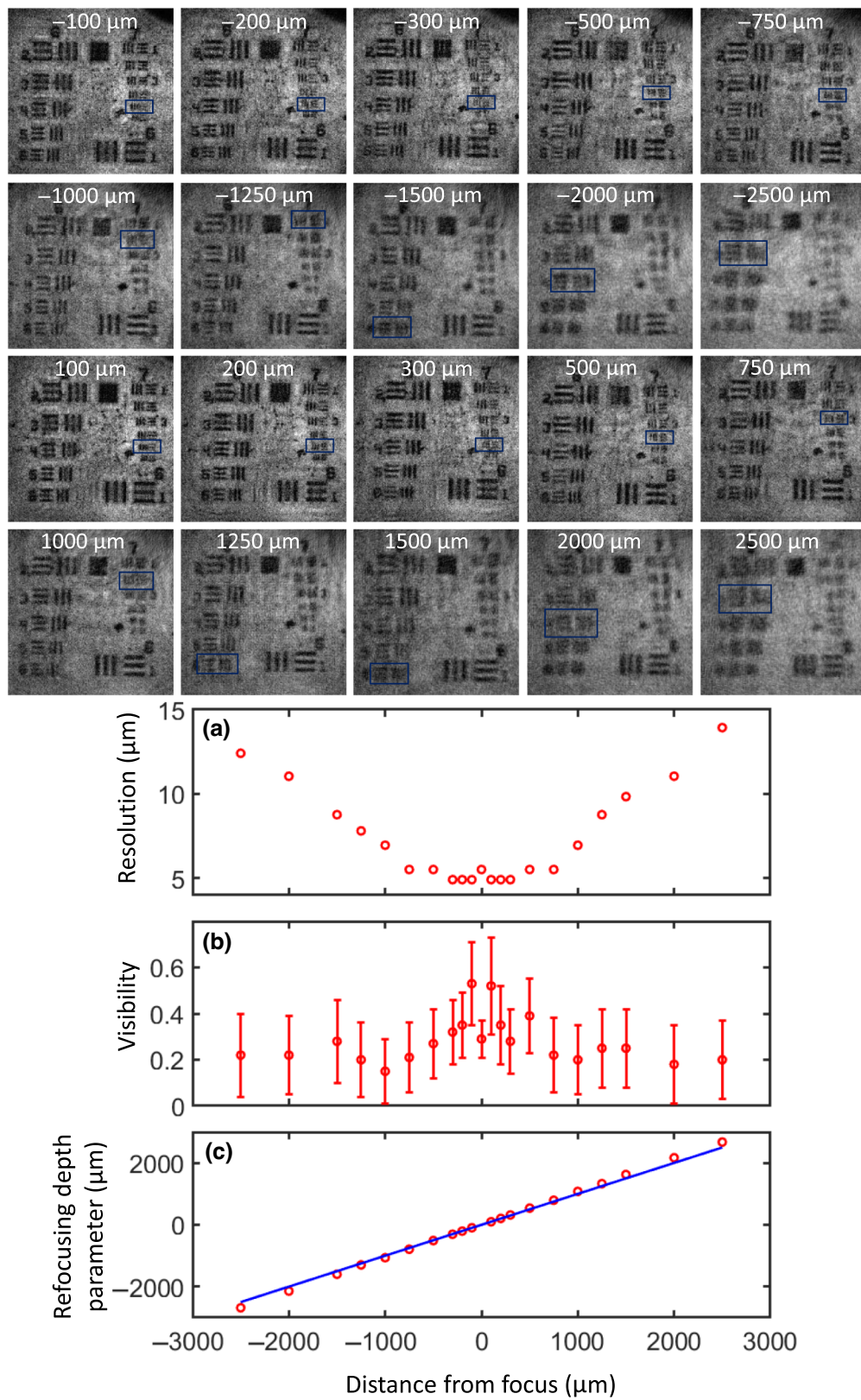


FIG. 7. Full dataset of Fig. 3 of the paper showing digitally refocused images of groups 6 and 7 of the 1951 USAF resolution target placed at various distances from the objective focus. (a),(b) shows the resolution and visibility of the smallest resolvable features (boxed in blue), respectively. (c) shows the depth parameter used for refocusing plotted against the actual distance at which the target is placed from the focus. Perfect agreement is indicated by the blue line.

propagating a distance z_0 . On the right-hand side, the first term is the intensity of the diffraction pattern of the target $|\tilde{f}(x,y,z_0)|^2$ as if obtained when illuminated by a plane wave traveling in the z direction. The second term is the intensity of the illuminating beam at $z = 0$, $|\sum_{n,m} U_{nm}(x + \Delta x_n, y + \Delta y_m, 0)|^2$, with each plane wave

also shifted by Δx_n and Δy_m in the x - y plane. If the intensity of the illuminating beam is uniform across the target then,

$$\sum_{n,m} \tilde{I}_{nm}(x + \Delta x_n, y + \Delta y_m, z_0) \propto |\tilde{f}(x,y,z_0)|^2. \quad (\text{A7})$$

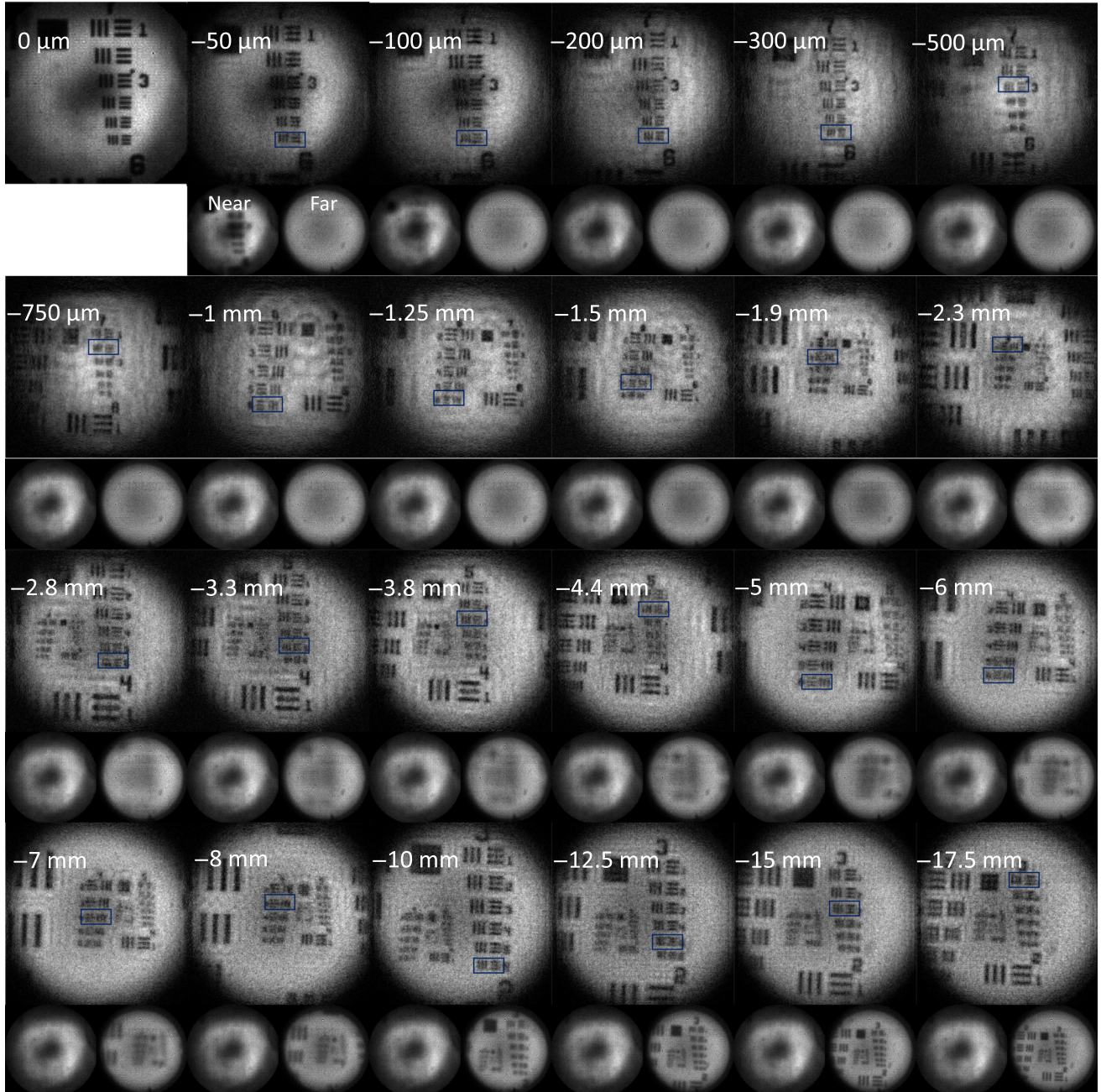


FIG. 8. Digitally refocused images of a 1951 USAF resolution target placed at various distances from the objective focus when using a 35-mm focal-length condenser lens. The centred resolution target group from 0 to $-750 \mu\text{m}$ away from the focus is group 7, -1 to -2.3 mm is group 6, -2.8 to -4.4 mm is group 5, -5 to -7 mm is group 4 and -10 to -17.5 mm is group 3. The smallest resolvable features after refocusing are boxed in blue. Images of the near-field crystal plane, imaged by the signal beam, and far-field crystal plane, imaged by the idler beam, before refocusing is shown below each refocused image.

Thus, with the amplitude of the diffraction pattern known and if we also know the phase profile of the target, the amplitude of the target can be retrieved using a Gerchberg-Saxton-type algorithm whose implementation is detailed in the main text.

APPENDIX B: MORE DETAILS ON THE EXPERIMENTAL SETUP

The schematic of the QCLFM setup is shown in Fig. 5(a) with most details given in the main text. The lenses in the signal beam were chosen such that the signal beam is not too tightly focused onto the sample region, allowing the field of view to stay roughly constant in the region of approximately ± 2 mm from the objective focus. When magnified onto the camera, the beam size should also roughly match the sensor area of the camera to ensure most photons will be captured. Likewise, in the idler beam, the lenses were chosen such that the idler beam will cover roughly a region of 100×100 pixels of the camera.

In order to achieve the highest degree of momentum correlation possible, a pair of lenses with focal length 100 and 150 mm were used to collimate and demagnify the laser beam to approximately 1 mm in diameter when hitting the PPKTP crystal. The expected degree of momentum correlation can be calculated as [48]

$$\sigma_{k_1+k_2} = \sqrt{1/l_c^2 + 1/(4\omega_p^2)}, \quad (\text{B1})$$

where $\sigma_{k_1+k_2}$ is the standard deviation in the momentum correlation between two photons with momentum k_1 and k_2 , l_c is the coherence length of the pump laser, and ω_p is the pump beam waist radius at the crystal. For our pump laser, $l_c \approx 200 \mu\text{m}$ and $\omega_p \approx 500 \mu\text{m}$, thus giving $\sigma_{k_1+k_2} \approx 5 \times 10^{-3} \mu\text{m}^{-1}$.

The experimental setup to perform momentum correlation measurement is shown in Fig. 5(b). Here, the Fourier

plane of the crystal is imaged by both the signal and idler photons, each onto a separate region of the camera. The common 200-mm lens is moved along the beam path until the highest degree of momentum correlation is observed. This setup is designed such that alteration of the idler path is kept to a minimum when converting to the QCLFM setup of Fig. 5(a). Momentum correlation measurement should be performed first in order to ensure that when converted to QCLFM, the camera is imaging the exact Fourier plane of the crystal, which would contain the highest degree of momentum correlation.

The measured momentum correlation, determined by fitting a Gaussian of the form $f(k) = a \exp\left(-\frac{(k-b)^2}{2\sigma_{k_1+k_2}^2}\right)$ to the central peak of the sum coordinate projection of the momentum joint probability distribution seen in Fig. 6(c), is $\sigma_{k_{x1}+k_{x2}} = 6.1 \times 10^{-3} \mu\text{m}^{-1}$ (0.90 pixels) and $\sigma_{k_{y1}+k_{y2}} = 6.4 \times 10^{-3} \mu\text{m}^{-1}$ (0.93 pixels) in the x and y direction, respectively. This is in agreement with the expected $5 \times 10^{-3} \mu\text{m}^{-1}$ as calculated using Eq. (B1).

APPENDIX C: TPX3CAM

The TPX3CAM has 256×256 pixels with a pixel pitch of $55 \mu\text{m}$. The pixels can individually time the arrival time of a light pulse with 1.6-ns accuracy. The camera is made single photon sensitive with an attached image intensifier in which a single photon is converted into a flash of light bright enough to be registered by the camera. The flash of light will illuminate a small cluster of pixels on the camera causing a slight blurring of the raw image data. It is therefore necessary to implement a clustering identification and centroiding algorithm to regroup each cluster into a single event. The timing of the camera pixels is intensity dependent, in which brighter pixels of a cluster will be registered as an earlier event than dimmer pixels of the same cluster, even though they are created from the same

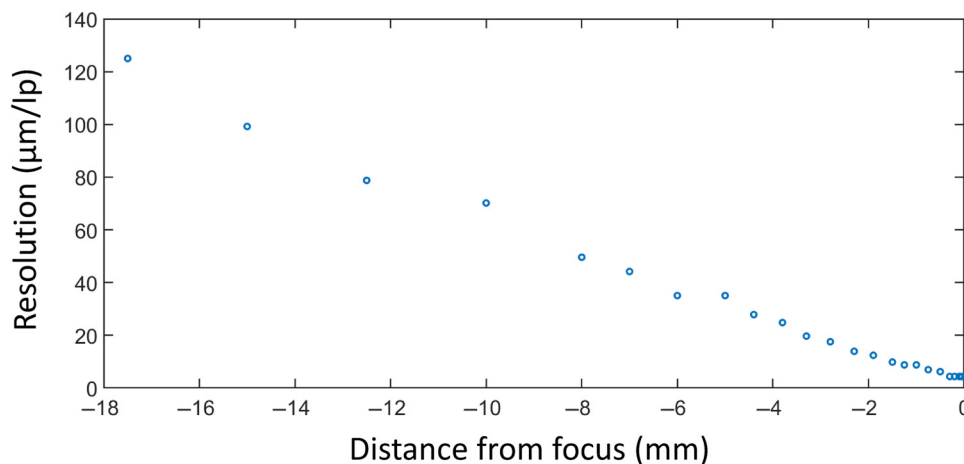


FIG. 9. Plot showing the smallest resolvable features versus the distance from focus for data shown in Fig. 8.

single-photon event. This intensity-dependent timing must also be corrected and will result in losing some timing accuracy giving an effective timing accuracy of approximately 8 ns. The quantum efficiency of the camera system (camera + intensifier) was measured to be approximately 7%. More details on the camera and the postprocessing required can be found in Refs. [41,49].

APPENDIX D: IMAGES OF FULL DATASET

All images for the dataset shown in Fig. 3(d) of the main paper shown in Fig. 7. The visibility of the smallest

resolvable features, defined as

$$V = \frac{I_{\max} - I_{\min}}{I_{\max} + I_{\min}}, \tag{D1}$$

is shown in Fig. 7(b). Here I_{\max} is the average maximum intensity of the bright region between the triplet bars and I_{\min} is the average minimum intensity of the dark region on the triplet bars. If V in one orientation of the triplet lines, whether vertical or horizontal, is greater than zero by more than the error bar then we consider it as resolved.

Figure 7(c) shows the depth parameter used for re-focusing against the actual distance at which the target is

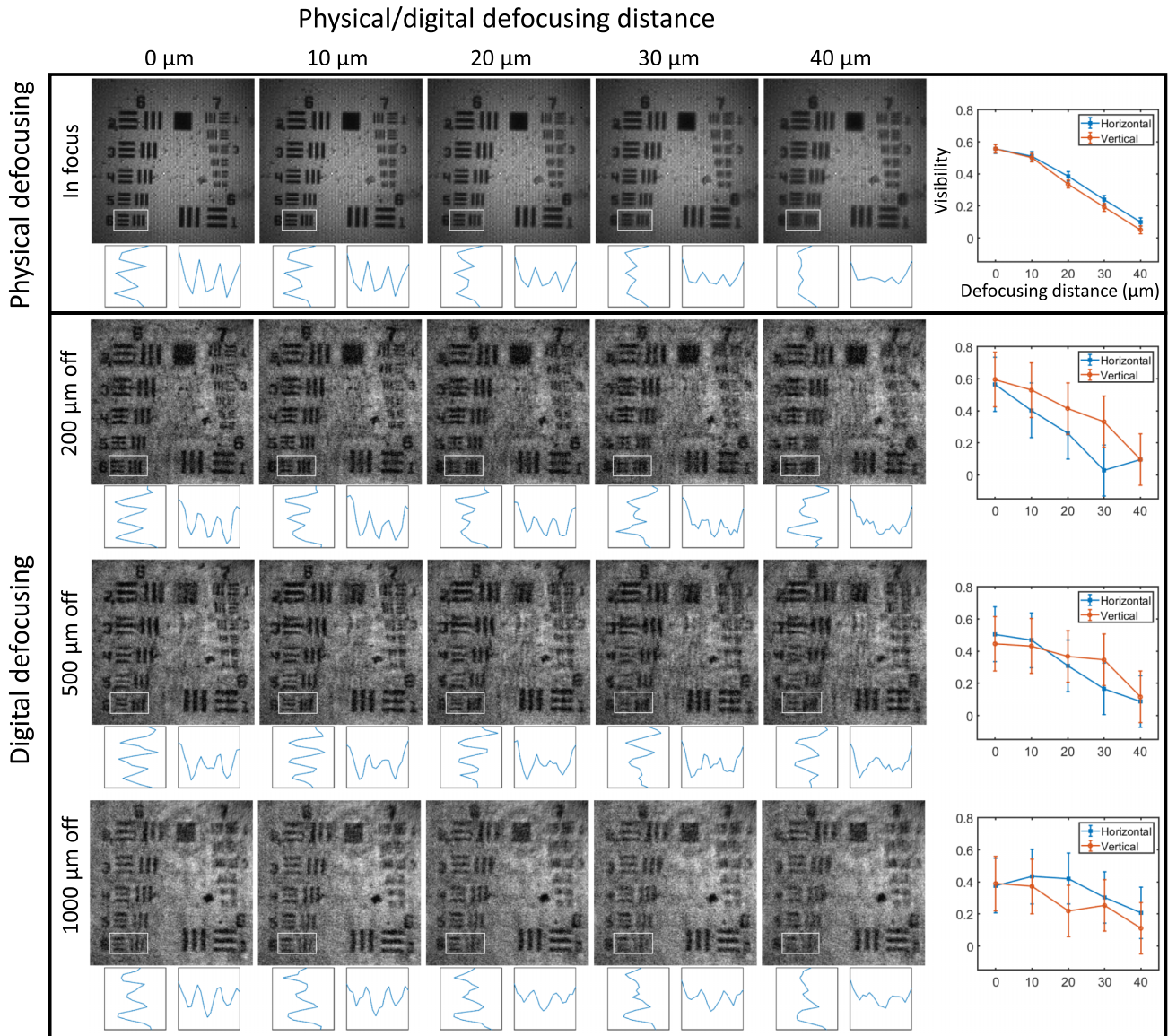


FIG. 10. Images demonstrating the axial resolution of QCLFM by comparing the point at which the triplet bars in the USAF target become unresolvable in a conventional microscope constructed using the same lenses, with the magnitude of digital refocusing required for the bars to become unresolvable. Under each image is the cross section of the horizontal and vertical triplet bars for the target group 6-6 with their corresponding visibility plotted on the side as a function of defocusing distance. The larger errorbars in the visibility of digitally refocused images is due to the low coincidence rate.

placed from the focus. The depth accuracy falls within a margin of error of approximately 2–8%. This current accuracy is obtained by fine tuning a single parameter, which is the focal length of the objective lens, during the ray-tracing step of the algorithm. We used the focal length values provided by the factory for all other lenses and assumed the distance between them to be precisely at the $4f$ imaging distances. Better accuracy can certainly be achieved through fine tuning additional parameters.

Figure 8 shows the dataset when using a 35-mm focal length condenser lens instead of the 100-mm condenser lens as used for Fig. 7. This configuration was chosen such that the smallest resolvable feature at each distance is close to the resolution limit of the camera. With this configuration, at the objective focus, the field of view (FOV) is approximately 1/3 of that when using a 100-mm condenser lens. However, the FOV expands much more rapidly with the 35 mm lens allowing larger target feature to better fit into the FOV when far away from the objective focus.

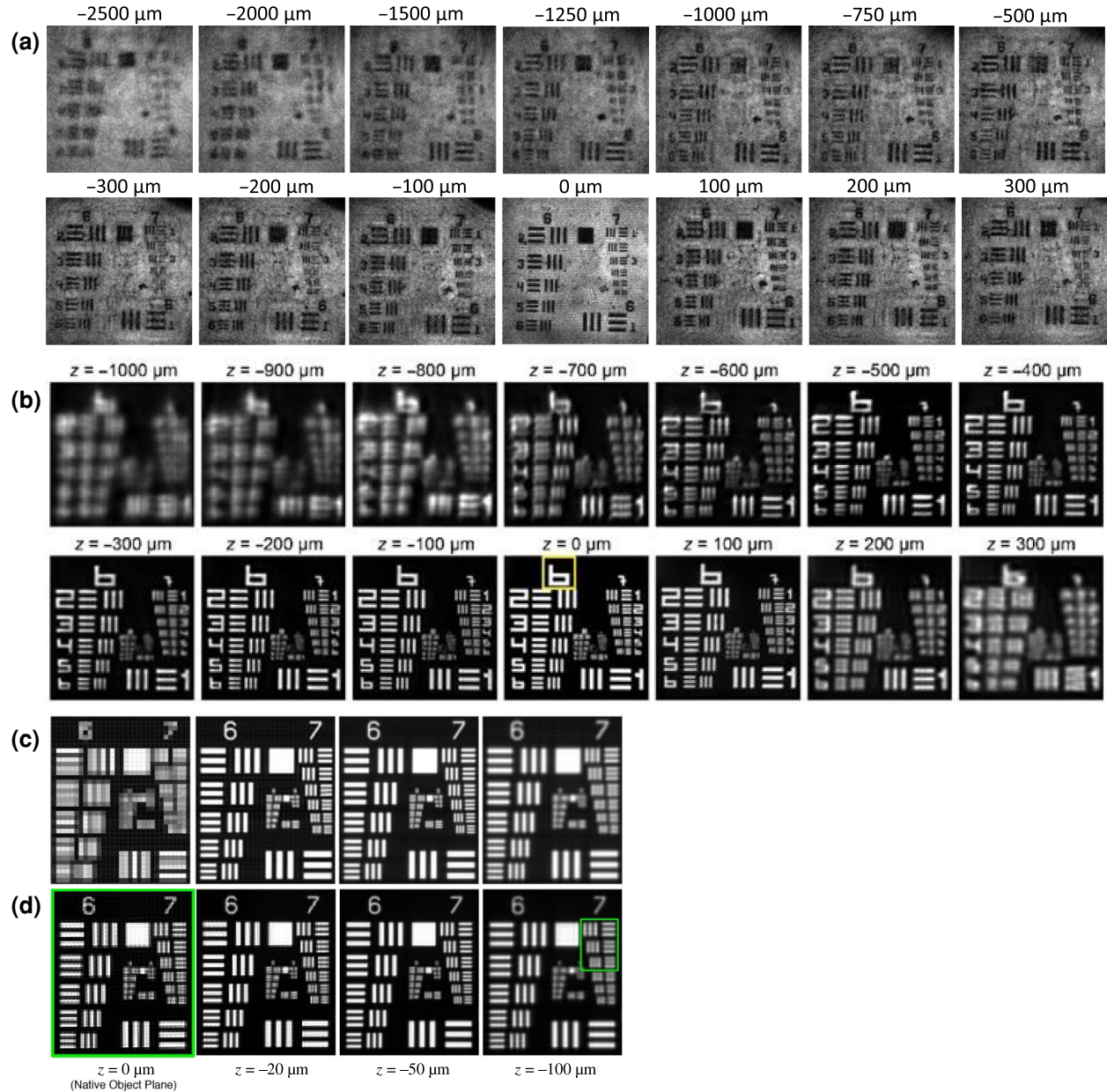
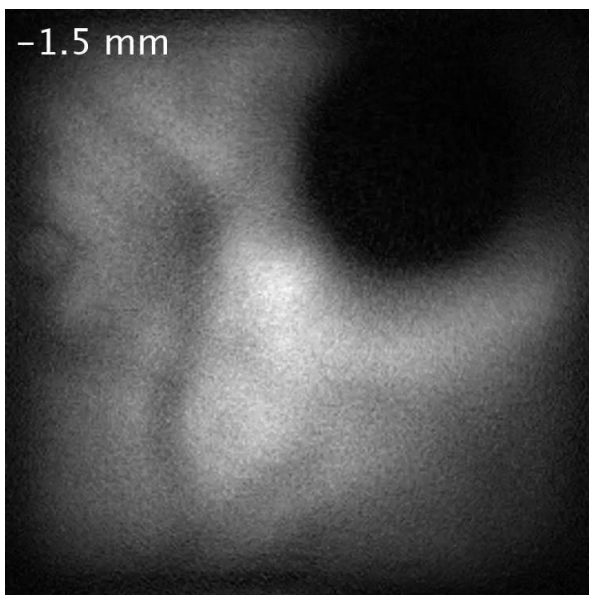


FIG. 11. Comparison of the refocusing distance between QCLFM and various conventional LFM techniques. (a) QCLFM, (b) results from Ref. [6] (Reprint permitted by the Creative Commons CC BY license), (c) results from Ref. [4] (Reprint and adapted with permission © The Optical Society), (d) results from Ref. [5] (Reprint and adapted with permission © The Optical Society).

In Fig. 8, we can see that beyond $-200\ \mu\text{m}$ away from the objective focus, the presence of the target can no longer be observed in the near field of the crystal plane imaged by the signal beam. From $-2.8\ \text{mm}$ away from the objective focus, the presence of the target can once again be observed through ghost imaging in the far field of the crystal plane imaged by the idler beam. A plot showing the smallest resolvable features versus the distance from focus is shown in Fig. 9.

APPENDIX E: AXIAL RESOLUTION OF QCLFM

The axial resolution of QCLFM is demonstrated in Fig. 10. Here, we placed the target at three different distances— 200 , 500 , and $1000\ \mu\text{m}$ —away from the focal plane, and digitally change the focusing by adjusting the depth parameter in our refocusing algorithm to see where the digitally refocused target becomes unresolvable again. This is then compared to a conventional microscope, constructed using the same lenses, where the target is now physically moved from the focus until it becomes unresolvable. By looking at the defocusing of the 1951 USAF target 6-6 we see that it becomes unresolvable at approximately $40\ \mu\text{m}$ when moved physically or digitally away from the focus, similarly for target 7-2, it becomes unresolvable at approximately $30\ \mu\text{m}$ when moved physically or digitally. Thus we can conclude that the axial resolution of QCLFM is comparable to the DOF of a conventional microscope constructed with the same lenses.



VIDEO 1. Video showing the digital refocusing of lens tissue fibers from a distance of -1.5 to $2.5\ \text{mm}$ away from the objective lens focus.

APPENDIX F: DOF COMPARISON WITH CONVENTIONAL LIGHT-FIELD MICROSCOPE DESIGNS

In Fig. 11 we compare the DOF of QCLFM with various light-field microscope demonstrations using the conventional microlens array-based designs. We can see our demonstration of QCLFM showed approximately a 10 times larger DOF when compared to Ref. [27] (group 7 element 3 with $1000\text{-}\mu\text{m}$ DOF compared to $100\text{-}\mu\text{m}$ DOF), which used 3D deconvolution, 5 times larger DOF when compared to Ref. [28] (group 7 element 4 with $500\text{-}\mu\text{m}$ DOF compared to $100\text{-}\mu\text{m}$ DOF), which used 3D deconvolution and wave-front shaping, and lastly a 3 times larger DOF when compared to Ref. [31], which utilized 3D deconvolution, image plane scanning, and spherical-aberration assistance.

APPENDIX G: VIDEO SHOWING THE DIGITAL REFOCUSING OF LENS TISSUE FIBERS

Video 1 shows the digital refocusing of an approximately 3-mm stack of lens cleaning tissue fibers from a distance of -1.5 to $2.5\ \text{mm}$ away from the objective lens focus.

-
- [1] G. Brida, M. Genovese, and I. Ruo Berchera, Experimental realization of sub-shot-noise quantum imaging, *Nat. Photonics* **4**, 227 (2010).
 - [2] Nigam Samantaray, Ivano Ruo-Berchera, Alice Meda, and Marco Genovese, Realization of the first sub-shot-noise wide field microscope, *Light: Sci. Appl.* **6**, e17005 (2017).
 - [3] T. B. Pittman, Y. H. Shih, D. V. Strekalov, and A. V. Sergienko, Optical imaging by means of two-photon quantum entanglement, *Phys. Rev. A* **52**, R3429 (1995).
 - [4] Jeffrey H. Shapiro and Robert W. Boyd, The physics of ghost imaging, *Quantum Inf. Process.* **11**, 949 (2012).
 - [5] Miles J. Padgett and Robert W. Boyd, An introduction to ghost imaging: Quantum and classical, *Philos. Trans. R. Soc. London, A: Math., Phys. Eng. Sci.* **375**, 20160233 (2017).
 - [6] Magued B. Nasr, Bahaa E. A. Saleh, Alexander V. Sergienko, and Malvin C. Teich, Demonstration of dispersion-canceled quantum-optical coherence tomography, *Phys. Rev. Lett.* **91**, 083601 (2003).
 - [7] Pablo Yepiz-Graciano, Zeferino Ibarra-Borja, Roberto Ramírez Alarcón, Gerardo Gutiérrez-Torres, Héctor Cruz-Ramírez, Dorilian Lopez-Mago, and Alfred B. U'Ren, Quantum optical coherence microscopy for bioimaging applications, *Phys. Rev. Appl.* **18**, 034060 (2022).
 - [8] Andrei Nomerotski, Imaging and time stamping of photons with nanosecond resolution in timepix based optical cameras, *Nucl. Instrum. Methods Phys. Res., Sect. A: Accelerators, Spectrometers, Detectors and Associated Equipment* **937**, 26 (2019).

- [9] Hugo Defienne, Jiuxuan Zhao, Edoardo Charbon, and Daniele Faccio, Full-field quantum imaging with a single-photon avalanche diode camera, *Phys. Rev. A* **103**, 042608 (2021).
- [10] Yingwen Zhang, Duncan England, Andrei Nomerotski, Peter Svihra, Steven Ferrante, Paul Hockett, and Benjamin Sussman, Multidimensional quantum-enhanced target detection via spectrotemporal-correlation measurements, *Phys. Rev. A* **101**, 053808 (2020).
- [11] Jiuxuan Zhao, Ashley Lyons, Arin Can Ulku, Hugo Defienne, Daniele Faccio, and Edoardo Charbon, Light detection and ranging with entangled photons, *Opt. Express* **30**, 3675 (2022).
- [12] Yingwen Zhang, Duncan England, and Benjamin Sussman, Snapshot hyperspectral imaging with quantum correlated photons, *Opt. Express* **31**, 2282 (2023).
- [13] Hazel Hodgson, Yingwen Zhang, Duncan England, and Benjamin Sussman, Reconfigurable phase contrast microscopy with correlated photon pairs, *Appl. Phys. Lett.* **122**, 034001 (2023).
- [14] Tomas Aidukas, Pavan Chandras Konda, Andrew R. Harvey, Miles J. Padgett, and Paul-Antoine Moreau, Phase and amplitude imaging with quantum correlations through Fourier ptychography, *Sci. Rep.* **9**, 10445 (2019).
- [15] Bienvenu Ndagano, Hugo Defienne, Dominic Branford, Yash D. Shah, Ashley Lyons, Niclas Westerberg, Erik M. Gauger, and Daniele Faccio, Quantum microscopy based on Hong–Ou–Mandel interference, *Nat. Photonics* **16**, 384 (2022).
- [16] Yingwen Zhang, Antony Orth, Duncan England, and Benjamin Sussman, Ray tracing with quantum correlated photons to image a three-dimensional scene, *Phys. Rev. A* **105**, L011701 (2022).
- [17] E. H. Adelson and J. Y. A. Wang, Single lens stereo with a plenoptic camera, *IEEE Trans. Pattern Anal. Mach. Intell.* **14**, 99 (1992).
- [18] R. Ng, M. Levoy, M. Bredif, G. Duval, M. Horowitz, and P. Hanrahan, Light field photography with a hand-held plenoptic camera, (2005). <https://raytrix.de/>.
- [19] <https://raytrix.de/>.
- [20] Marc Levoy, Ren Ng, Andrew Adams, Matthew Footer, and Mark Horowitz, Light field microscopy, *ACM Trans. Graph.* **25**, 924 (2006).
- [21] Oliver Bimber and David Schedl, Light-field microscopy: A review, *J. Neurol. Neuromedicine* **4**, 1 (2019).
- [22] Depeng Wang, Zhijing Zhu, Zhongyuan Xu, and Diming Zhang, Neuroimaging with light field microscopy: A mini review of imaging systems, *The European Physical Journal Special Topics* **231**, 749 (2022).
- [23] A. Orth, M. Ploschner, E. R. Wilson, I. S. Maksymov, and B. C. Gibson, Optical fiber bundles: Ultra-slim light field imaging probes, *Sci. Adv.* **5**, eaav1555 (2019).
- [24] David C. Schedl and Oliver Bimber, Volumetric light-field excitation, *Sci. Rep.* **6**, 29193 (2016).
- [25] Young-Tae Lim, Jae-Hyeung Park, Ki-Chul Kwon, and Nam Kim, Resolution-enhanced integral imaging microscopy that uses lens array shifting, *Opt. Express* **17**, 19253 (2009).
- [26] Antony Orth and Kenneth Crozier, Microscopy with microlens arrays: High throughput, high resolution and light-field imaging, *Opt. Express* **20**, 13522 (2012).
- [27] Michael Broxton, Logan Grosenick, Samuel Yang, Noy Cohen, Aaron Andalman, Karl Deisseroth, and Marc Levoy, Wave optics theory and 3-D deconvolution for the light field microscope, *Opt. Express* **21**, 25418 (2013).
- [28] Noy Cohen, Samuel Yang, Aaron Andalman, Michael Broxton, Logan Grosenick, Karl Deisseroth, Mark Horowitz, and Marc Levoy, Enhancing the performance of the light field microscope using wavefront coding, *Opt. Express* **22**, 24817 (2014).
- [29] Xing Lin, Jiamin Wu, Guoan Zheng, and Qionghai Dai, Camera array based light field microscopy, *Biomed. Opt. Express* **6**, 3179 (2015).
- [30] Changliang Guo, Wenhao Liu, Xuanwen Hua, Haoyu Li, and Shu Jia, Fourier light-field microscopy, *Opt. Express* **27**, 25573 (2019).
- [31] Yi Zhang, Yuling Wang, Mingrui Wang, Yuduo Guo, Xinyang Li, Yifan Chen, Zhi Lu, Jiamin Wu, Xiangyang Ji, and Qionghai Dai, Multi-focus light-field microscopy for high-speed large-volume imaging, *PhotonIX* **3**, 30 (2022).
- [32] Milena D’Angelo, Francesco V. Pepe, Augusto Garuccio, and Giuliano Scarcelli, Correlation plenoptic imaging, *Phys. Rev. Lett.* **116**, 223602 (2016).
- [33] Francesco V. Pepe, Francesco Di Lena, Augusto Garuccio, Giuliano Scarcelli, and Milena D’Angelo, Correlation plenoptic imaging with entangled photons, *Technologies* **4**, 17 (2016).
- [34] Francesco Di Lena, Francesco V. Pepe, Augusto Garuccio, and Milena D’Angelo, Correlation plenoptic imaging: An overview, *Appl. Sci.* **8**, 1958 (2018).
- [35] Francesco V. Pepe, Francesco Di Lena, Aldo Mazzilli, Eitan Edrei, Augusto Garuccio, Giuliano Scarcelli, and Milena D’Angelo, Diffraction-limited plenoptic imaging with correlated light, *Phys. Rev. Lett.* **119**, 243602 (2017).
- [36] Gianlorenzo Massaro, Davide Giannella, Alessio Scagliola, Francesco Di Lena, Giuliano Scarcelli, Augusto Garuccio, Francesco V. Pepe, and Milena D’Angelo, Light-field microscopy with correlated beams for high-resolution volumetric imaging, *Sci. Rep.* **12**, 16823 (2022).
- [37] Gianlorenzo Massaro, Paul Mos, Sergii Vasiukov, Francesco Di Lena, Francesco Scattarella, Francesco V. Pepe, Arin Ulku, Davide Giannella, Edoardo Charbon, Claudio Bruschini, and Milena D’Angelo, Correlated-photon imaging at 10 volumetric images per second, *Sci. Rep.* **13**, 12813 (2023).
- [38] <https://www.amscins.com/tpx3cam/>.
- [39] R. W. Gerchberg, A practical algorithm for the determination of phase from image and diffraction plane pictures, *Optik* **35**, 237 (1972).
- [40] J. R. Fienup, Phase retrieval algorithms: A comparison, *Appl. Opt.* **21**, 275 (1982).
- [41] Victor Vidyapin, Yingwen Zhang, Duncan England, and Benjamin Sussman, Characterisation of a single photon event camera for quantum imaging, *Sci. Rep.* **13**, 1009 (2023).
- [42] Fabio Severini, Iris Cusini, Francesca Madonini, Davide Brescia, Robin Camphausen, Álvaro Cuevas, Simone Tisa, and Federica Villa, Spatially resolved event-driven 24×24 pixels SPAD imager with 100 duty cycle for low optical power quantum entanglement detection, *IEEE J. Solid-State Circuits* **58**, 2278 (2023).

- [43] G. Brida, M. V. Chekhova, G. A. Fornaro, M. Genovese, E. D. Lopaeva, and I. Ruo Berchera, Systematic analysis of signal-to-noise ratio in bipartite ghost imaging with classical and quantum light, *Phys. Rev. A* **83**, 063807 (2011).
- [44] G. Kim, K. Park, K. T. Lim, J. Kim, and G. Cho, Improving spatial resolution by predicting the initial position of charge-sharing effect in photon-counting detectors, *J. Instrum.* **15**, C01034 (2020).
- [45] Agedi N. Boto, Pieter Kok, Daniel S. Abrams, Samuel L. Braunstein, Colin P. Williams, and Jonathan P. Dowling, Quantum interferometric optical lithography: Exploiting entanglement to beat the diffraction limit, *Phys. Rev. Lett.* **85**, 2733 (2000).
- [46] Milena D'Angelo, Maria V. Chekhova, and Yanhua Shih, Two-photon diffraction and quantum lithography, *Phys. Rev. Lett.* **87**, 013602 (2001).
- [47] <https://global.canon/en/news/2021/20211215.html>.
- [48] Hugo Defienne and Sylvain Gigan, Spatially entangled photon-pair generation using a partial spatially coherent pump beam, *Phys. Rev. A* **99**, 053831 (2019).
- [49] Arthur Zhao, Martin van Beuzekom, Bram Bouwens, Dmitry Byelov, Irakli Chakaberia, Chuan Cheng, Erik Maddox, Andrei Nomerotski, Peter Svihra, Jan Visser, Vaclav Vrba, and Thomas Weinacht, Coincidence velocity map imaging using Tpx3Cam, a time stamping optical camera with 1.5 ns timing resolution, *Rev. Sci. Instrum.* **88**, 113104 (2017).